COMBINED ROOF INTERSTORY SHEAR ENERGY STORAGE MODEL AND ANALYSIS OF INFLUENCING FACTORS

Peng-Fei Zhang, Yan Tan, Lei Guo, Tong-Bin Zhao, Zhen-xin Wei

College of Energy and Mining Engineering, Shandong University of Science and Technology, Qingdao, China
e-mail: 15064221133@163.com (Peng-fei Zhang); tanyan.ty@qq.com (corresponding author Yan Tan);
1920365481@qq.com (Lei Guo); ztbwh2001@126.com (Tong-bin Zhao); 1484539823@qq.com (Zhen-xin Wei)

To reveal the shear deformation and energy storage mechanism of composite roof strata, and to quantify the interlayer shear energy storage characteristics of composite roof strata, this study establishes a shear energy mechanical model for layered composite roof structures under various conditions. The factors influencing the shear energy storage of rock strata are analyzed, and the energy release process as well as mechanism of layered composite roof strata are discussed, leading to the following conclusions: the shear strain energy linearly increases with an increase in bond layer thickness and quadratically increases with increasing external forces. During the bending deformation stage, when thick and hard layers exist in composite beams, shear failure dominated by interlayer shear slip occurs, and low-strength rock beams exhibit tensile crack initiation. In the overall instability stage, the composite beams mainly experience tensile fracture. When thick and hard layers exist in the composite beams, the fracture strength and released energy are higher. The presence of thick and hard layers in the roof is a key factor leading to severe structural damage and increased energy release.

Keywords: roof, interlayer shear, energy, composite beam model, influencing factors

1. Introduction

The hard roof is a type of roof above the coal seam that is characterized by strong integrity, high strength, and large thickness, accumulating a significant amount of elastic energy. It is a typical geological condition in coal mining engineering that can trigger dynamic ground pressure incidents (He *et al.*, 2012; Małkowski and Niedbalski, 2020; Tan *et al.*, 2018; Yang *et al.*, 2019). The movement and fracturing of the roof caused by coal mining lead to structural damage of the roof, releasing a large amount of stored energy, which is one of the root causes of induced dynamic disasters in mining areas. The complex and diverse characteristics of the roof above the coal seam lead to bending deformation and subsequent fracturing under the load of overlying strata. Throughout this process, the energy storage during bending deformation and the energy release during fracture of the roof structure are crucial for the prevention of dynamic ground pressure disasters (Tajdus *et al.*, 2018; Cui *et al.*, 2020; Xu *et al.*, 2021; Li *et al.*, 2022; Zhou *et al.*, 2023). Therefore, the mechanism of energy release in the destruction of hard roof structures has been an important research topic for mining scholars both domestically and internationally.

The bending and fracturing of the roof structure is a complex process influenced by various factors such as roof thickness (Lu *et al.*, 2019), physical and mechanical properties (Coggan *et al.*, 2012; Xu *et al.*, 2023), joint development characteristics (Bai and Tu, 2020), contact forms, and combined movement patterns (Shen *et al.*, 2019; Yu *et al.*, 2022). Extensive research has been conducted by scholars on the roof structure model in mining areas, proposing hypotheses such as the pressure arch hypothesis (Xia *et al.*, 2018), the "cantilever beam" hypothesis

(Han *et al.*, 2015), the hinged rock block hypothesis (Qin *et al.*, 2021), and the "natural balance arch" hypothesis (Han *et al.*, 2015), providing preliminary insights into the "zonation structure" of the roof. To further elucidate the mechanism of roof fracturing, scholars have developed mechanical structural models represented by beams (Ti *et al.*, 2021), plates (Wang *et al.*, 2022), and arch shells (Liu and Shi, 2021). For example, the "transmission rock beam", "masonry beam" structural models, and the "key layer theory" (Cao and Huang, 2021) have quantitatively solved the fracturing step distance of roof rock beams. In order to further study the coordinated movement laws of multi-layer roofs, scholars have introduced basic concepts such as the composite roof, composite key layer, and key layer group (Zhang *et al.*, 2021; Qi *et al.*, 2022; Wang *et al.*, 2023), investigating the fracturing laws of multi-layer composite roof structures under mining influence, including weakly bonded composite roofs, composite fragmentation, and multiple key layers of overlying rock (Liu *et al.*, 2021; Zhang *et al.*, 2023), revealing the composite effects and fracturing mechanisms of the roof.

In summary, valuable research findings have been obtained by domestic and foreign scholars regarding the bending and fracturing of composite roofs, including the roof structure models, fracturing mechanisms, and composite movement characteristics. However, the mechanical properties of interlayer contact surfaces in the roof significantly affect the integrity, flexural moment capacity, and fracturing distance of the composite roof. Most of the current research is limited to studying the fracture of the roof rock mass itself, while the shear instability mechanism of composite roofs has not been investigated, and a mechanical model describing the shear energy storage problem of composite roofs has not been established. This makes it difficult to quantitatively calculate the energy storage under such conditions. Therefore, this study establishes a shear energy storage mechanical model for layered composite roof structures under different conditions. From a theoretical perspective, it reveals the shear deformation and energy storage mechanisms of composite roofs and analyzes the factors influencing the shear energy storage of rock layers. This study provides a theoretical basis for the prevention and control of impact ground pressure caused by roof fracturing.

2. The stress analysis of the composite roof

In mining areas, certain relatively hard and thick rock layers are referred to as key strata (Lu *et al.*, 2020). These key strata are composed of single layers or adjacent multiple layers of hard rock, gradually forming a load-bearing structure in the mining area with the extraction of coal, playing a crucial control role in the overlying rock layers. When the key strata are formed by two layers of rock together, this load-bearing structure can be simplified as a composite beam that only bears the load of the overlying rock layers before the key strata fracture, as shown in Fig. 1.
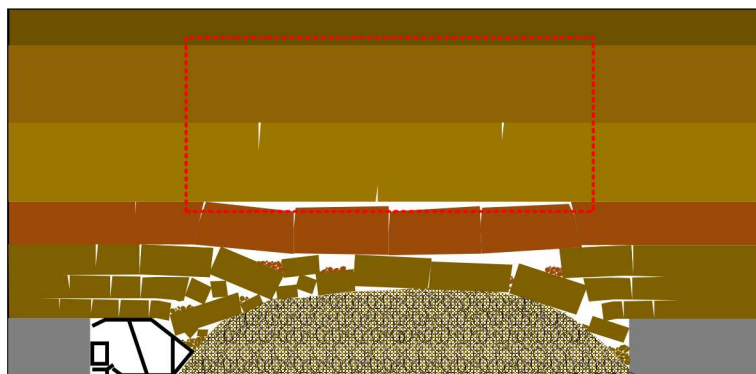

Fig. 1. Schematic diagram of the combined roof structure

Assuming the load provided by the overlying rock layers is a concentrated load, this segment of the composite beam becomes a lateral bending beam. According to the plane assumption, the normal stress on the cross-section of a rectangular section beam during bending deformation is

$$\sigma = \frac{My}{I_z} \tag{2.1}$$

where σ is the normal stress on the cross-section of a rectangular section beam, M is the equivalent bending couple exerted by the overlying rock, y is the distance from any point to the neutral axis, I_z is the moment of inertia of the rock beam.

The rock layers in the roof strata often exhibit variations in the lithology due to different geological formation periods. The interfaces between these rock layers are cemented together. Therefore, before relative sliding occurs between adjacent rock layers, the two adjacent roof layers can be treated as a double-layer composite beam structure. Assuming that the upper and lower layers of the beam consist of different lithologies with elastic moduli of E_1 and E_2, and thicknesses of h_1 and h_2, respectively, as shown in Fig. 2, the expressions for the shear force and bending moment in the beam are given by Eq. (2.2)

$$
\begin{aligned}
F_S(x) &= \begin{cases} \dfrac{P}{2} & 0 \leqslant x < \dfrac{S}{2} \\[2mm] -\dfrac{P}{2} & \dfrac{S}{2} \leqslant x < S \end{cases} \\[4mm]
M(x) &= \begin{cases} \dfrac{Px}{2} & 0 \leqslant x < \dfrac{S}{2} \\[2mm] \dfrac{PS}{2} - \dfrac{Px}{2} & \dfrac{S}{2} \leqslant x \leqslant S \end{cases}
\end{aligned}
\tag{2.2}
$$

where $F_S(x)$ is the shear force distribution function in the beam, $M(x)$ is the bending moment distribution function in the beam, P is the concentrated load on the upper part of the rock beam, S is the span of the rock beam, and x is the horizontal position coordinate of any point in the beam.
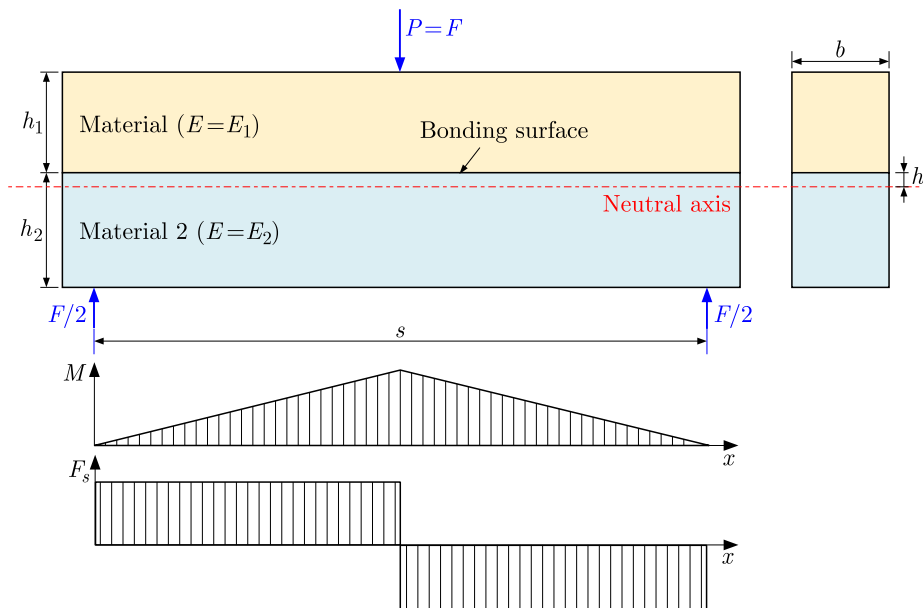

Fig. 2. Schematic diagram of force analysis of the composite beam

Based on the plane assumption, it can be inferred that the longitudinal strain at any point y along the height of the cross-section of the composite beam varies linearly. The longitudinal strain at point y is given by

$$\varepsilon = \frac{y}{\rho} \tag{2.3}$$

where ε is the longitudinal strain, ρ is the radius of curvature of the neutral axis.

3. Shear energy storage model for composite roof strata layers

3.1. Interlayer slip criterion

In order to analyze the mechanical properties at the interface of the composite beam, according to the method of equivalent sections, the cross-section of the composite beam is transformed equivalently into a beam with varying widths but made of the same material. This section is referred to as the equivalent section, as shown in Fig. 3.
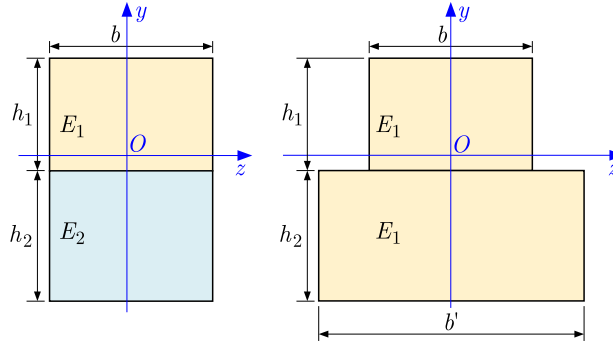

Fig. 3. Schematic diagram of the equivalent section of the composite beam

The moment of inertia of the equivalent section can be calculated as follows

$$I_z' = I_{z1} + \eta I_{z2} \tag{3.1}$$

where I_z' is the moment of inertia of the equivalent section; I_{z1} is the moment of inertia of the lower beam section, I_{z2} is the moment of inertia of the lower beam section, η is the ratio of elastic modulus between the lower and the upper beam, $\eta = E_2/E_1$.

Therefore, the static equilibrium equation for the equivalent section can be expressed as

$$\int_{A_1} y_1 \, dA + \int_{A_2} \eta y_2 \, dA = 0 \tag{3.2}$$

where y_1 is the distance from the upper beam point to the neutral axis, A_1 is the section area of the upper rock beam, y_2 is the distance from the upper beam point to the neutral axis, A_2 is the section area of the lower rock beam.

According to formula (3.2), the flexural shear stress on the upper and lower beam sections is

$$\tau_1 = \frac{F_S S_Z^*}{b I_z'} \qquad \tau_2 = \frac{\eta F_S S_Z^*}{b I_z'} \tag{3.3}$$

where b is the width of the composite beam, F_S is the shear force on the cross section, $F_S = F/2$, S_Z^* is the static moment of the area outside the cross section h' away from the neutral axis with respect to the neutral axis, $S_Z^* = b(h_1^2 - h'^2)/2$.

According to the theorem of mutual equivalence of shear stress, the shear stress at the interface of the composite beam is

$$\tau' = \tau_1 - \tau_2 = (1 - \eta)\frac{F_S S_Z^*}{b I_z'} \tag{3.4}$$

where τ' is the shear stress at the interface of the composite beam, τ_1 is the flexural shear stress on the upper beam sections, τ_1 is the flexural shear stress on the lower beam sections.

In the test, the upper limit of τ' depends on the interfacial shear strength of the bond surface. In the actual stratum, τ' refers to the shear stress of the interlayer area of adjacent rock layers. If the shear strength of the cementing area is $[\tau]$, then according to the third strength theory, the criterion for shear slip of the bonding surface of the composite beam is as follows

$$\tau' \geqslant [\tau] \tag{3.5}$$

By bringing formula (3.4) into formula (3.5), the shear slip criterion of the bonded surface of the composite beam can be obtained as follows

$$P \geqslant \frac{4(I_{z1} + \eta I_{z1})[\tau]}{(1 - \eta)(h_1^2 - h'^2)} \tag{3.6}$$

where h' is the distance from the boundary of the rock beam to the neutral axis, h_1 is the thickness of the upper beam.

When formula (3.6) is satisfied, the composite beam exhibits shear slip along the bonding surface between rock layers.

3.2. Interlayer shear energy storage

When composite beams are subjected to interlaminar shear stress, the stored shear strain energy mainly concentrates on the bonding surface. In the test, the energy storage area is the bonding layer between the composite beam rock layers, and in the real stratum, it is the interlayer area of the lithology change. According to the calculation formula of shear strain energy density, the shear strain energy density is

$$dU_{\varepsilon\tau} = \frac{\tau \, dx \, dz \, \gamma \, dy}{2} = \frac{\tau^2}{2G} \, dx \, dy \, dz \tag{3.7}$$

where $dU_{\varepsilon\tau}$ is the shear strain energy density stored in composite beams, τ is the shear stress of the bonded surface of the composite beam, γ is the shear strain of the bonded surface of the composite beam.

Therefore, the shear strain energy of the bonded surface of the composite beam is as follows

$$U_{\varepsilon\tau} = \iiint\limits_{v_\varepsilon} \frac{\tau^2}{2G} \, dv_\varepsilon = \int_0^{h_b} \int_0^b \int_0^S \frac{\tau^2}{2G} \, dx \, dy \, dz \tag{3.8}$$

where $U_{\varepsilon\tau}$ is the shear strain energy stored in composite beams, v_ε is the volume of bonded surface of composite beam, h_b is the thickness of the bonding zone, G is the shear modulus of the bond.

Assuming that the shear stress on the bonding surface is uniformly distributed, the above formula can be simplified as follows

$$U_{\varepsilon\tau} = \frac{\tau^2}{2G} h_b b S = \frac{h_b b S}{2G} \left[\frac{(1 - \eta)(h_i^2 - h'^2)}{4(I_{z1} + \eta I_{z1})} P \right]^2 \tag{3.9}$$

Formula (3.9) is the expression form of the interlayer shear energy storage model of the composite beam. When no shear slip occurs between the composite beams, the stored shear strain energy can be calculated according to Eq. (3.9). When interlayer shear slip occurs, the maximum shear strain energy stored by the composite beam is as follows

$$U_{\varepsilon\tau} = \frac{[\tau]^2}{2G} h_b b S \tag{3.10}$$

3.3. Analysis of influencing factors

In order to analyze the influence of various factors on the shear energy storage, a numerical model of composite beam FLAC3D was established. A total of 42 groups of numerical models were established. The schematic diagram of the model is shown in Fig. 4, and the simulation parameters are listed in Table 1.
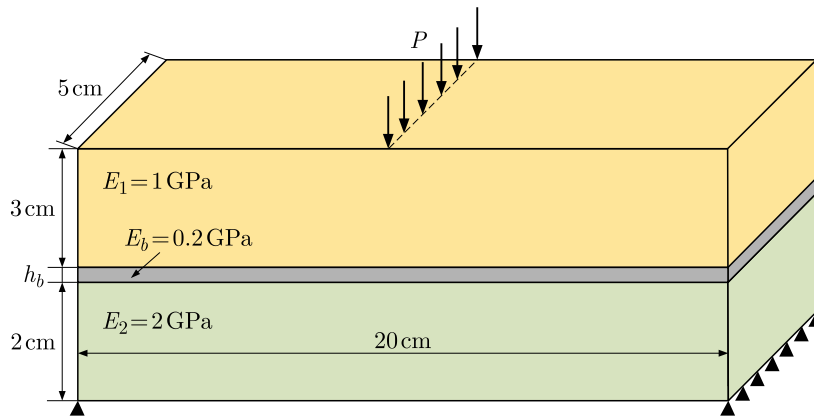

Fig. 4. Schematic diagram of the numerical model

Table 1. Parameter values from numerical simulation

Number	P [kN]	h_b [cm]	Number	P [kN]	h_b [cm]	Number	P [kN]	h_b [cm]
1	0.5	0.10	15	0.5	0.30	29	2.0	0.05
2	1.5	0.10	16	1.5	0.30	30	2.0	0.15
3	2.5	0.10	17	2.5	0.30	31	2.0	0.25
4	3.5	0.10	18	3.5	0.30	32	2.0	0.35
5	4.0	0.10	19	4.0	0.30	33	2.0	0.40
6	4.5	0.10	20	4.5	0.30	34	2.0	0.45
7	5.0	0.10	21	5.0	0.30	35	2.0	0.50
8	0.5	0.20	22	1.0	0.05	36	3.0	0.05
9	1.5	0.20	23	1.0	0.15	37	3.0	0.15
10	2.5	0.20	24	1.0	0.25	38	3.0	0.25
11	3.5	0.20	25	1.0	0.35	39	3.0	0.35
12	4.0	0.20	26	1.0	0.40	40	3.0	0.40
13	4.5	0.20	27	1.0	0.45	41	3.0	0.45
14	5.0	0.20	28	1.0	0.50	42	3.0	0.50

Figure 5 and Table 2 show the calculation results of shear strain energy in numerical simulation. When other conditions remain unchanged, the shear strain energy increases linearly with an increase of cementation layer thickness, indicating that the thicker the cementation
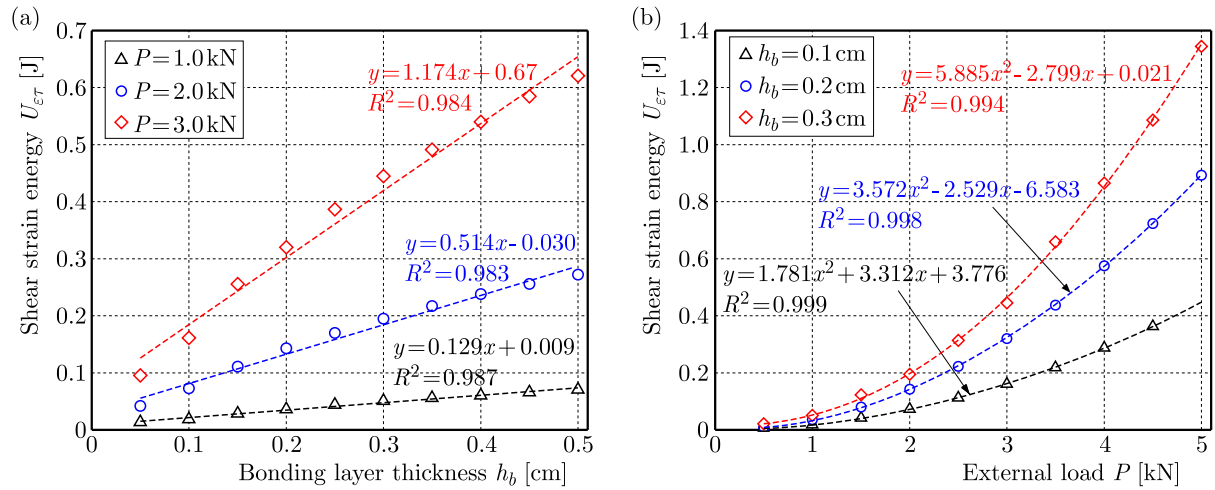
Fig. 5. Numerical simulation results: (a) influence of the bonding layer thickness, (b) influence of the external load

Table 2. Shear strain energy values

Number	Shear strain energy [J]	Number	Shear strain energy [J]	Number	Shear strain energy [J]
1	0.00464	15	0.02154	29	0.04183
2	0.04162	16	0.12246	30	0.11107
3	0.11230	17	0.31403	31	0.17074
4	0.21886	18	0.65948	32	0.21673
5	0.28728	19	0.86494	33	0.23807
6	0.36265	20	1.08598	34	0.25600
7	0.44718	21	1.34482	35	0.27199
8	0.00810	22	0.01333	36	0.09551
9	0.08012	23	0.02859	37	0.25554
10	0.22331	24	0.04398	38	0.38651
11	0.43689	25	0.05571	39	0.49136
12	0.57522	26	0.06003	40	0.54014
13	0.72299	27	0.06557	41	0.58462
14	0.89271	28	0.07057	42	0.62091

layer in the composite beam, the more shear strain energy can be stored. With an increase of the external force, the shear strain energy increases as a quadratic polynomial, indicating that the external force applied by the composite beam is greater, and the stored shear strain energy will increase accordingly.

4. Energy release process of the laminated composite roof

In order to analyze the energy storage characteristics of composite beam samples, a three-point bending test of a double-layer composite beam was carried out (Fig. 6). The samples are mainly composed of limestone and fine sandstone, and their basic mechanical properties are listed in Table 3. Before the test, the limestone and fine sandstone samples were cut into samples with a length of 200 mm and a width of 40 mm, and the sample heights were 20 mm/30 mm/40 mm, respectively. The cut samples were bonded by gypsum to make the samples of different combinations. The sample numbers and parameters are listed in Table 4.
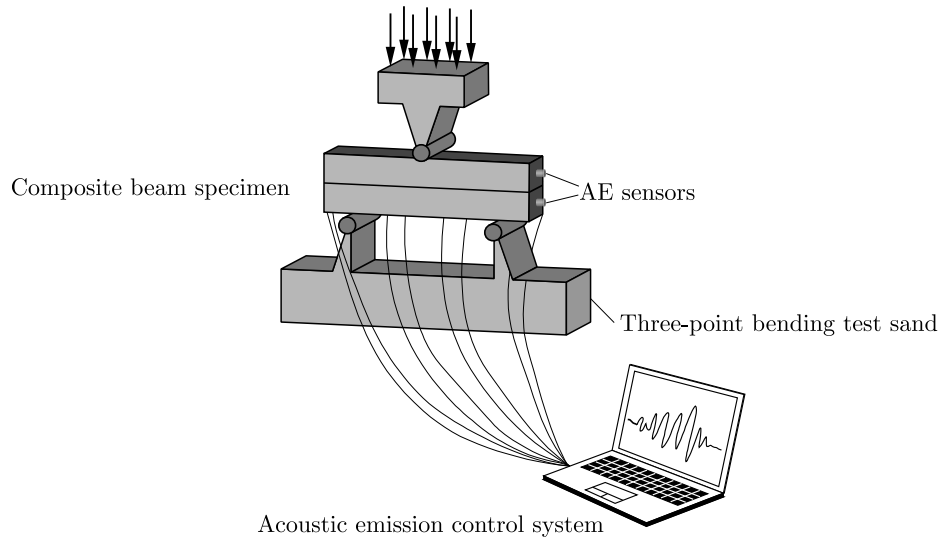
Fig. 6. Schematic diagram of three-point bending test of the composite beam

Table 3. Basic physical and mechanical parameters of composite beams

Lithology	Density ρ [g·cm^{-3}]	Compressive strength σ_c [MPa]	Tensile strength σ_t [MPa]	Modulus of elasticity E [GPa]	Shear wave velocity c_s [m·s^{-1}]	Longitudinal wave velocity c_p [m·s^{-1}]
Fine sandstone	2.65	78.23	7.64	7.51	2615.22	4102.69
Limestone	2.39	62.45	5.62	5.38	2203.17	3223.75

Table 4. Composite beam test plan

Sample number	Upper lithology	Upper layer thickness h_1 [mm]	Underlying lithology	Underlayer thickness h_2 [mm]
40S-20H	Fine sandstone	40	Limestone	20
40H-20S	Limestone	40	Fine sandstone	20
30S-30H	Fine sandstone	30	Limestone	30
30H-30S	Limestone	30	Fine sandstone	30
20S-40H	Fine sandstone	20	Limestone	40
20H-40S	Limestone	20	Fine sandstone	40

The loading system adopts the RLJW-2000 servo-controlled rock pressure testing machine of Shandong University of Science and Technology. The displacement loading method is adopted in the test. The loading rate is set at 0.05 mm/min, the sampling frequency is 10 Hz, and the span is set at 150 mm. In order to analyze the fracture characteristics of composite beams during loading, an acoustic emission test was carried out simultaneously. The acoustic emission testing equipment is AMSY-6 acoustic emission system produced by Vallen Company. Before the test, eight WS45-H acoustic emission probes were arranged on the surface of the sample to collect the acoustic emission signals during the failure process of the sample, and the acoustic emission positioning was carried out. The position of acoustic emission probe is shown in Fig. 7.

The acoustic emission signals generated during the failure of composite beam specimens are caused by the fracture of specimens. The fracture in rock interior is mainly the tensile crack caused by the tensile stress, and the fracture at the interface is mainly the shear crack
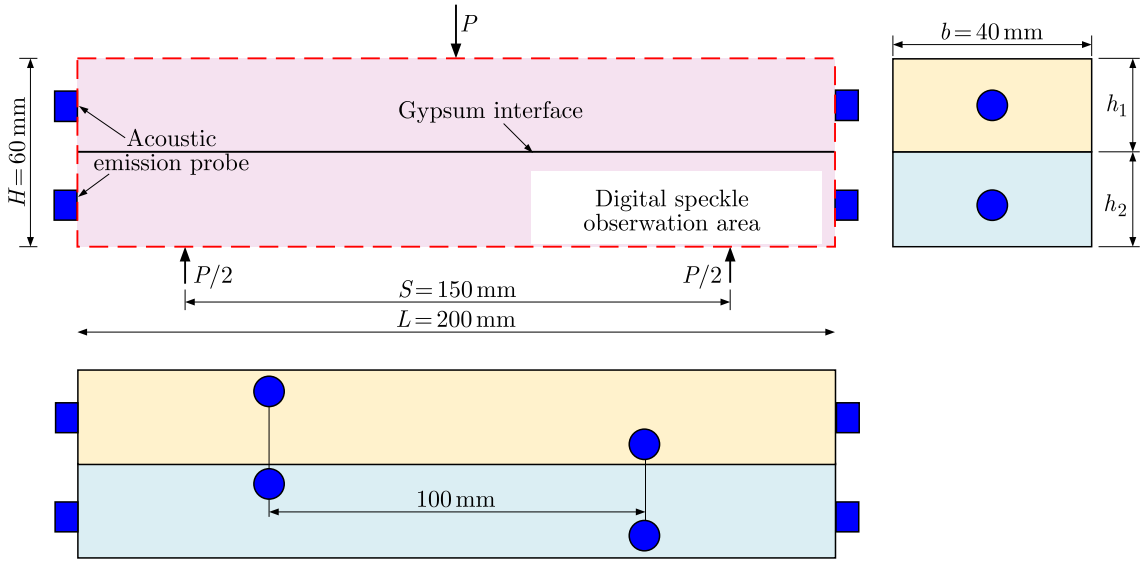
Fig. 7. Schematic diagram of sensor layout

caused by the bending shear stress. Therefore, it is of great significance to reveal the complete process of composite beam rupture by analyzing the distribution law of acoustic emission signals associated with the fracture of different mechanisms during specimen loading, and establishing the corresponding relationship between the fracture type, occurrence time and sound emission signal energy.

In the field of acoustic emission research, RA and AF distribution changes based on time-domain parameters can qualitatively describe the composition of shear cracks and tensile cracks in samples during the development stage of rock fracture, and then determine the evolution law of different types of cracks. RA and AF can be calculated according to formulas (4.1) and (4.2). In Japan's JC MS-III B5706 concrete building Code, the slope of AF/RA sector-line is defined as k, the signal of AF/RA $< k$ is defined as a shear fracture signal, and the signal of AF/RA $\geqslant k$ is defined as a tensile fracture signal. Although the partition parameter k of shear and tensile fracture is greatly different due to the influence of rock material and sensor type, the method of calculating the proportion of rock fracture type based on k value is valid according to the research results of many papers. In this Section, the research results from literature (Ohno and Ohtsu, 2010) are adopted, $k = 80$ is used as the dividing standard of shear and tensile fracture, that is, formula (4.3), and the test results of 6 groups are analyzed

$$\text{AF} = \frac{C}{D} \tag{4.1}$$

where C is the acoustic emission count, D is the duration of acoustic emission

$$\text{RA} = \frac{R}{A} \tag{4.2}$$

where R is the rise time of acoustic emission, A is the acoustic emission amplitude

$$\text{Crack type} = \begin{cases} \text{tensile crack} & \dfrac{\text{AF}}{\text{RA}} \geqslant 80 \\[2ex] \text{shear crack} & \dfrac{\text{AF}}{\text{RA}} < 80 \end{cases} \tag{4.3}$$

Figure 8 shows the number of two types of cracks and the corresponding energy distribution in the loading process of six groups of samples as can be seen from the figure.
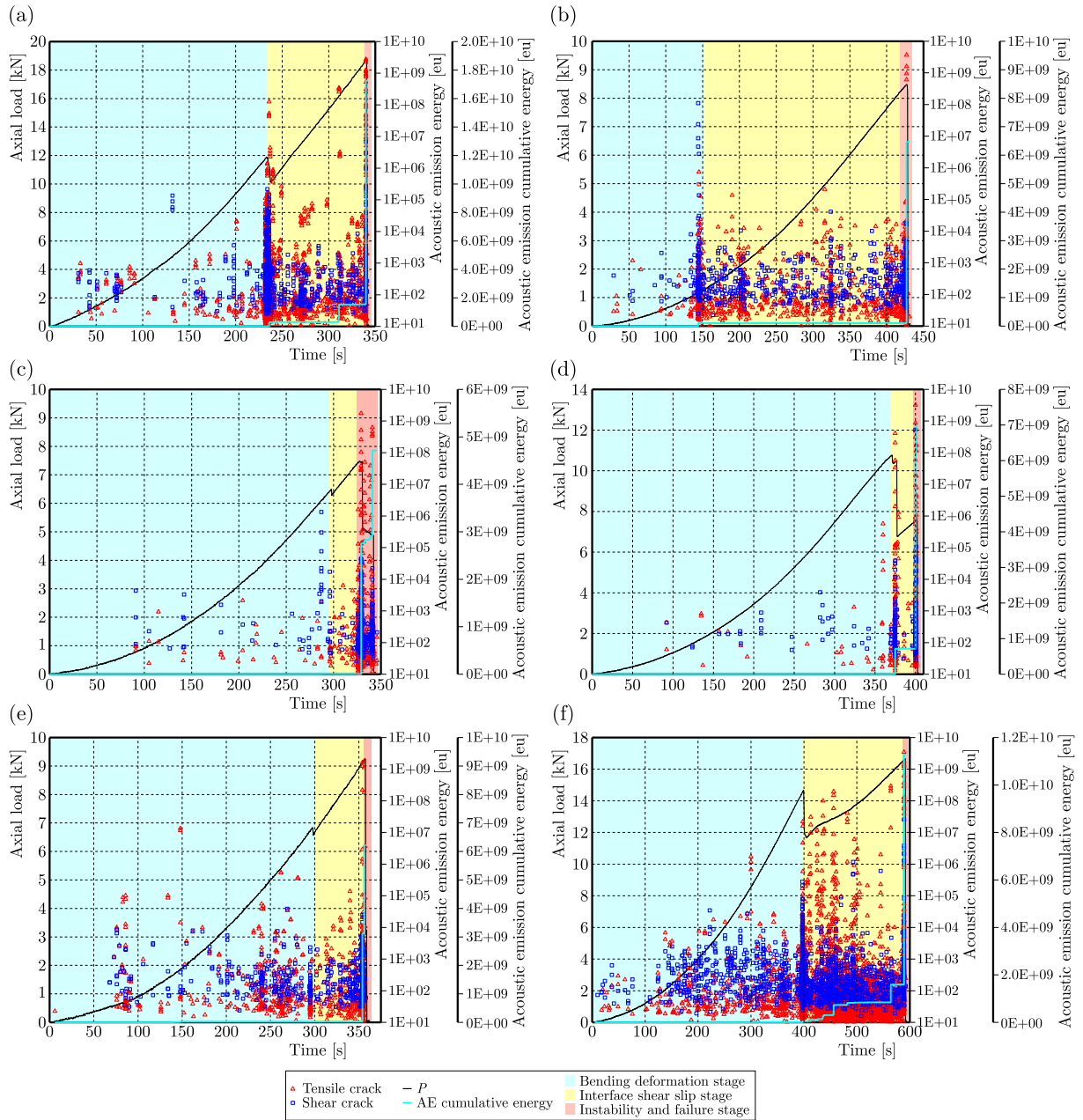
Fig. 8. Acoustic emission energy curve of composite beam: (a) 40S-20H, (b) 40H-20S, (c) 30S-30H, (d) 30H-30S, (e) 20S-40H, (f) 20H-40S

According to the loading time and acoustic emission curve in Fig. 8, it is divided into three stages: the overall bending deformation stage (blue background in the figure), the interface friction slip stage (yellow background in the figure), and the instability fracture stage (red background in the figure). In the six groups of tests, two concentrated areas of high energy acoustic emission events appeared almost simultaneously, which were located at the end of the overall bending deformation stage and the overall instability fracture stage, respectively, indicating that relatively severe macroscopic cracks appeared in the samples when the composite beams were loaded to two time nodes. In the early stage of loading, a small amount of two kinds of acoustic emission fracture signals appeared in the composite beam sample, indicating that the internal fracture of the sample in the early stage of loading is a mixture of internal tensile fracture and interface shear fracture.

The two types of composite beams have great differences in the acoustic emission energy. The total energy released by 40H-20S, 30S-30H and 20S-40H samples without thick and hard layers is 6.47×10^9eu, 4.71×10^9eu and 6.23×10^9eu, respectively. The total energy released by samples with thick hard layer in 40S-20H, 30H-30S and 20H-40S is 1.73×10^{10}eu, 7.00×10^{10}eu and 1.13×10^{10}eu, respectively. When there is a thick hard layer in the composite beam, the total energy of AE signal and the number of high energy AE signal increase significantly. The results show that the existence of the thick hard layer makes the internal fracture of the composite beam significantly increase the acoustic emission activity, rupture strength and energy release of the composite beam.

There are great differences in crack types between the two types of composite beams, which are mainly reflected in the following aspects: the cracks of composite beams without thick hard layers (samples 40H-20S, 30S-30H, 20S-40H) are mainly shear fracture in the overall bending deformation stage, indicating that shear failure occurs at the rock layer interface under the action of shear stress, and the interlayer shear slip occurs at this time. The composite beams containing thick hard layers (samples 40S-20H, 30H-30S, 20H-40S) show high energy tensile fracture at the same time in the concentration area of the first high energy acoustic emission event, indicating that when the composite beams contain thick hard layers, in addition to shear failure mainly caused by shear slip at the interface, tensile cracks in the rock also appear at this stage. This phenomenon occurs mostly in low-strength rock beams, and corresponds to the results of a digital speckle test. When the samples were loaded to the stage of overall instability, the acoustic emission signals were mainly of the tensile type. At this stage, the composite beam samples were overall unstable, and the two layers of rock beams both experienced the tensile fracture, indicating that the energy source in this stage was almost all from the tensile failure inside the rock mass.

To sum up, the thick hard layer in the roof is the key factor leading to a severe damage degree of the composite structure and an increase of energy release. In the prevention and control of rock burst, we should pay attention to this part of rock formation, and reduce the effective size and elastic modulus to diminish the purpose of weakening the fracture strength.

5. Discussion

According to the physical function relationship, the rock fracture process meets

$$U_s = W + V \tag{5.1}$$

where U_s is the total strain energy stored during rock loading, W is the fracture work done by rock crack formation, V is the energy released by rock failure.

Under the condition of composite beams, the total strain energy stored can be expressed as

$$U_s = U_{\varepsilon\tau} + U_{\varepsilon b} \tag{5.2}$$

where $U_{\varepsilon b}$ is bending strain energy stored in the composite beams.

Similarly, the energy V released by failure of the composite beam can be expressed as

$$V = V_b + V_\tau \tag{5.3}$$

where V_b is the energy release when bending and breaking, V_τ is the shear failure energy release.

Therefore, the functional relationship in the fracture process of composite beams can be expressed as

$$U_{\varepsilon\tau} + U_{\varepsilon b} = W + V_\tau + V_b \tag{5.4}$$

In fracture mechanics, the fracture work is a parameter to evaluate how much energy is consumed when a rock breaks, reflecting the energy required for fracture expansion, which can be obtained from the load-displacement curve (P-δ curve) measured by the three-point bending test and the area surrounded by the horizontal coordinate. Due to the limitation of test conditions, the posterior peak of the P-δ curve is generally difficult to measure directly, and it is approximately considered to conform to the law of power function, which can be expressed as

$$P = \beta \delta^{-\lambda} \tag{5.5}$$

where β and λ are curve coefficients, which can be determined by fitting the test data points after $P = P_{max}/3$, and the displacement at this time is set as δ_1.

Assuming that the end of the P-δ curve extends to an infinite displacement, the fracture work can be expressed as

$$
\begin{aligned}
W = W_0 + W_1 + W_G &= \int_0^{\delta_1} P(\delta)\,d\delta + \int_{\delta_1}^{+\infty} \beta \delta^{-\lambda}\,d\delta + mg\delta_0 \\
&= \int_0^{\delta_1} P(\delta)\,d\delta + \frac{\beta}{1-\lambda}\delta_1 + mg\delta_0
\end{aligned}
\tag{5.6}
$$

where W_0 is the envelope area of the measured P-δ curve at $0 \leqslant \delta < \delta_1$ and the horizontal coordinate, W_1 is the envelope area of the measured P-δ curve at $\delta > \delta_1$ and the horizontal coordinate, W_G does work for the body weight of the specimen, δ_0 is the mid-span displacement of the composite beam.

6. Conclusion

To reveal the shear deformation and energy storage mechanism of composite roof strata, quantify the interlayer shear energy storage characteristics of composite roof strata, this study establishes a shear energy mechanical model of layered composite roof structures under different conditions. Factors influencing the rock strata shear energy storage are analyzed, the energy release process and mechanism of layered composite roof strata are discussed, leading to the following conclusions:

- The shear strain energy linearly increases with an increase in bond layer thickness and quadratically increases with increasing external forces.
- During the bending deformation stage, when thick and hard layers exist in the composite beams, shear failure dominated by interlayer shear slip occurs, and low-strength rock beams exhibit tensile crack initiation. In the overall instability stage, the composite beams mainly experience tensile fracture.
- When thick and hard layers exist in composite beams, the fracture strength and released energy are higher. The presence of thick and hard layers in the roof is a key factor leading to severe structural damage and increased energy release.
- In the prevention of dynamic rock burst, special attention should be paid to this part of thick and hard rock strata, aiming to weaken the fracture strength by reducing effective dimensions and decreasing elastic modulus.
- In the future research, a bending loading device suitable for triaxial conditions can be designed and developed according to the real ground stress environment, and corresponding tests can be carried out to reveal the influence of ground stress environment on the fracture characteristics of the roof.

References

1. BAI Q., TU S., 2020, Numerical observations of the failure of a laminated and jointed roof and the effective of different support schemes: A case study, *Environmental Earth Sciences*, **79**, 202

2. CAO J., HUANG Q., 2021, Roof structure of shallow coal seam group mining in Western China, *Plos One*, **16**, 8

3. COGGAN J., GAO F., STEAD D., ELMO D., 2012, Numerical modelling of the effects of weak immediate roof lithology on coal mine roadway stability, *International Journal of Coal Geology*, **90-91**, 100-109

4. CUI F., YANG Y., LAI X., JIA C., SHAN P., 2020, Experimental study on the effect of advancing speed and stoping time on the energy release of overburden in an upward mining coal working face with a hard roof, *Sustainability*, **12**, 1, 37

5. HAN C.L., ZHANG N., LI B.Y., SI G.Y., ZHENG X.G., 2015, Pressure relief and structure stability mechanism of hard roof for gob-side entry retaining, *Journal of Central South University*, **22**, 4445-4455

6. HE J., DOU L.M., CAO A.Y., GONG S.Y., LÜ J.W., 2012, Rock burst induced by roof breakage and its prevention, *Journal of Central South University*, **19**, 1086-1091

7. LI W., TU S., TU H., LIU X., MIAO K., *et al.*, 2022, A new method to assess thick, hard roof-induced rock burst risk based on mining speed effect on key energy strata, *Sustainability*, **14**, 22, 15054

8. LIU J., LI C., SHI Y., ZHANG Y., 2021, Stability analysis and fracture patterns of hard main roof in longwall top coal caving with large mining height, *Shock and Vibration*, **2021**

9. LIU W., SHI Q., 2021, Study on evolution characteristics and instability model of overburden stress shell with the longwall mining along strike, *Shock and Vibration*, **2021**

10. LU W., HE C., ZHANG X., 2020, Height of overburden fracture based on key strata theory in longwall face, *Plos One*, **15**, 1

11. LU Y., GONG T., XIA B., YU B., HUANG F., 2019, Target stratum determination of surface hydraulic fracturing for far-field hard roof control in underground extra-thick coal extraction: A case study, *Rock Mechanics and Rock Engineering*, **52**, 8, 2725-2740

12. MAŁKOWSKI P., NIEDBALSKI Z., 2020, A comprehensive geomechanical method for the assessment of rockburst hazards in underground mining, *International Journal of Mining Science and Technology*, **30**, 3, 345-355

13. OHNO K., OHTSU M., 2010, Crack classification in concrete based on acoustic emission, *Construction and Building Materials*, **24**, 12, 2339-2346

14. QI F., YANG D., LI X., LI B., ZHAI Y., YU S., 2022, Study on roof presplitting mechanism and deformation control of reused roadway in compound soft rock by roof presplitting approach, *Geofluids*, **2022**, 1, 144937

15. QIN G., CAO J., WANG C., WU S., ZHAI M., 2021, Characteristics of stratum structure and fracture evolution in stratified mining of shallow buried high-gas-thick coal seam by similarity simulation, *Geofluids*, **2021**, 1, 555451

16. SHEN W., WANG M., CAO Z., SU F., NAN H., LI X., 2019, Mining-induced failure criteria of interactional hard roof structures: A case study, *Energies*, **12**, 15, 3016

17. TAJDUS A., CALA M., TAJDUS K., 2018, Seismicity and rock burst hazard assessment in fault zones: A case study, *Archives of Mining Sciences*, **63**, 3, 747-765

18. TAN Y.L., LIU X.S., SHEN B., NING J.G., GU Q.H., 2018, New approaches to testing and evaluating the impact capability of coal seam with hard roof and/or floor in coal mines, *Geomechanics and Engineering*, **14**, 4, 367-376

19. TI Z., LI J., WANG M., WANG K., JIN Z., TAI C., 2021, Fracture mechanism in overlying strata during longwall mining, *Shock and Vibration*, **2021**

20. WANG H., JIAO J., WU Y., ZHENG K., LI Y., WANG T., JIANG B., 2023, Deformation characteristics and stress evolution law of composite hard roof under presplitting weakening, *Mining, Metallurgy & Exploration*, **40**, 839-850

21. WANG X., LU M., WEI R., WANG Z., LI S., 2022, Mechanical mechanism analysis of roof fracture evolution in stope with variable length based on elastic-plastic structure theory, *Geofluids*, **2022**, 1, 475021

22. XIA B., ZHANG X., YU B., JIA J., 2018, Weakening effects of hydraulic fracture in hard roof under the influence of stress arch, *International Journal of Mining Science and Technology*, **28**, 6, 951-958

23. XU C., YANG G., SUN H., QIN L., WANG K., *et al.*, 2021, Key strata inducing dynamic disasters based on energy condition: Criterion and application, *Geofluids*, **2021**, 1, 672020

24. XU D.Q., ZHANG P.S., YAN W., ZHANG X.L., DONG Y.H., NIU H., 2023, Mechanical properties and energy of sandstone under cyclic loading in evolutionary pattern experimental studies, *Archives of Mining Sciences*, **68**, 2, 351-370

25. YANG Z., LIU C., ZHU H., XIE F., DOU L., CHEN J., 2019, Mechanism of rock burst caused by fracture of key strata during irregular working face mining and its prevention methods, *International Journal of Mining Science and Technology*, **29**, 6, 889-897

26. YU M., ZUO J., SUN Y., MI C., LI Z., 2022, Investigation on fracture models and ground pressure distribution of thick hard rock strata including weak interlayer, *International Journal of Mining Science and Technology*, **32**, 1, 137-153

27. ZHANG J., HE Y., YANG T., BAI W., WU J., *et al.*, 2023, Coevolution mechanism and branch of pillar-overburden fissures in shallow coal seam mining, *Energy Science & Engineering*, **11**, 5, 1630-1642

28. ZHANG J., WANG B., BAI W., YANG S., 2021, A study on the mechanism of dynamic pressure during the combinatorial key strata rock column instability in shallow multi-coal seams, *Advances in Civil Engineering*, **2021**

29. ZHOU K.Y., MAŁKOWSKI P., DOU L.M., YANG K., CHAI Y.J., 2023, Using elastic wave velocity anomaly to predict rockburst hazard in coal mines, *Archives of Mining Sciences*, **68**, 1, 141-164